Clim. Past, 19, 787–802, 2023
https://doi.org/10.5194/cp-19-787-2023

Climate of the Past
Open Access
EGU

Lipid-biomarker-based sea surface temperature record offshore Tasmania over the last 23 million years

Suning Hou, Foteini Lamprou, Frida S. Hoem, Mohammad Rizky Nanda Hadju, Francesca Sangiorgi, Francien Peterse, and Peter K. Bijl

Department of Earth Sciences, Utrecht University, Utrecht, 3584CB, the Netherlands

Correspondence: Suning Hou (s.hou@uu.nl)

Received: 29 September 2022 – Discussion started: 4 October 2022
Revised: 19 January 2023 – Accepted: 10 March 2023 – Published: 4 April 2023

Abstract. The Neogene (23.04–2.58 Ma) is characterised by progressive buildup of ice volume and climate cooling in the Antarctic and the Northern Hemisphere. Heat and moisture delivery to Antarctica is, to a large extent, regulated by the strength of meridional temperature gradients. However, the evolution of the Southern Ocean frontal systems remains scarcely studied in the Neogene. Here, we present the first long-term continuous sea surface temperature (SST) record of the subtropical front area in the Southern Ocean at Ocean Drilling Program (ODP) Site 1168 off western Tasmania. This site is, at present, located near the subtropical front (STF), as it was during the Neogene, despite a 10° northward tectonic drift of Tasmania. We analysed glycerol dialkyl glycerol tetraethers (GDGTs – on 433 samples) and alkenones (on 163 samples) and reconstructed the paleotemperature evolution using TEX_{86} and $U_{37}^{k'}$ as two independent quantitative proxies. Both proxies indicate that Site 1168 experienced a temperate ∼ 25 °C during the early Miocene (23–17 Ma), reaching ∼ 29 °C during the mid-Miocene climatic optimum. The stepwise ∼ 10 °C cooling (20–10 °C) in the mid-to-late Miocene (12.5–5.0 Ma) is larger than that observed in records from lower and higher latitudes. From the Pliocene to modern (5.3–0 Ma), STF SST first plateaus at ∼ 15 °C (3 Ma), then decreases to ∼ 6 °C (1.3 Ma), and eventually increases to the modern levels around ∼ 16 °C (0 Ma), with a higher variability of 5° compared to the Miocene. Our results imply that the latitudinal temperature gradient between the Pacific Equator and the STF during late Miocene cooling increased from 4 to 14 °C. Meanwhile, the SST gradient between the STF and the Antarctic margin decreased due to amplified STF cooling compared to the Antarctic margin. This implies a narrowing SST gradient in the Neogene, with contraction of warm SSTs and northward expansion of subpolar conditions.

1 Introduction

Sea surface temperature (SST) reconstructions (Rousselle et al., 2013; Zhang et al., 2014; Herbert et al., 2016; Sangiorgi et al., 2018; Super et al., 2018, 2020; Tanner et al., 2020; Van der Weijst et al., 2022) and benthic foraminiferal oxygen isotopes (Lewis et al., 2007; Holbourn et al., 2013; Lear et al., 2015; Westerhold et al., 2020; Leutert et al., 2021) demonstrated that Neogene climate cooling occurred stepwise, with episodes of intermittent warming, e.g. during the mid-Miocene climatic optimum (MCO, 16.9–15 Ma) and the mid-Pliocene warm period (mPWP, 3.264–3.025 Ma). This cooling trend is further accompanied by Antarctic ice volume increase (Lewis et al., 2007; Lear et al., 2015; Leutert et al., 2021), pCO_2 decline (Sosdian et al., 2018; Super et al., 2018; Tanner et al., 2020; Rae et al., 2021), strengthening of the Antarctic Circumpolar Current (ACC; Sijp et al., 2014; Evangelinos et al., 2022) and sea ice expansion (McKay et al., 2012; Bijl et al., 2018; Sangiorgi et al., 2018), e.g. during the mid-Miocene climatic transition (MMCT, 14.5–12.5 Ma). The Southern Ocean is of special importance in reconstructions of past climate, as it plays a crucial role in ocean circulation and ocean–atmosphere carbon exchange and as a modulator of heat transport towards the largest body of land ice on Earth, the Antarctic ice sheet (Rintoul et al., 2018). The latitudinal position and strength of the ACC and its associated ocean fronts are forced by position shifts of the westerlies and bathymetry and have been suggested to modulate ocean–atmosphere CO_2 exchange as a feedback to the climate system (Toggweiler et al., 2006; Skinner et al., 2010). The gradual widening of the Tasmanian Gateway and the Drake Passage in the Neogene provided the geographic boundary conditions for a further strengthening of the ACC and associated oceanic fronts (Sijp et al., 2014; Evangelinos et al., 2022). Yet, the evolution of the ACC in the Neogene is poorly documented, as its strength and position are difficult to constrain from geological archives. One of the manifestations of a strengthening ACC and frontal systems would be an increase in the meridional temperature gradient in the Southern Ocean, particularly the gradient between the Antarctic margin and the subtropical front (STF). The latter represents the northern limit of the Southern Ocean, the northern branch of the ACC, and the boundary between the subtropical gyre and the subpolar waters, representing an oceanographic midpoint between the Equator and Antarctica. While individual SST reconstructions for the Neogene Southern Ocean exist (e.g. Herbert et al., 2016), the evolution of the latitudinal SST gradient has thus far not been evaluated. Although a compilation of Antarctic ice-proximal SSTs has recently become available (Duncan et al., 2022), SST reconstructions from the more northern parts of the Southern Ocean only cover short time intervals, which precludes an integrated overview of the evolution of the latitudinal SST gradient.

Here, we provide a detailed reconstruction of the Neogene SST evolution of the subtropical front based on lipid biomarkers stored in sediments retrieved from Ocean Drilling Program (ODP) Site 1168, offshore western Tasmania. We base our reconstruction on two independent SST proxies. The TEX_{86} paleothermometer is based on the relative number of cyclopentane moieties in isoprenoid glycerol dialkyl glycerol tetraethers (isoGDGTs) produced by marine archaea, which varies as a function of ambient temperature in a global set of marine surface sediments (Schouten et al., 2002). The $U^{k'}_{37}$ index is based on the relative abundance of di- and tri-unsaturated C_{37} alkenones synthesised by unicellular haptophyte marine algae, which yield a robust relationship with SST (Volkman et al., 1980; Eglinton and Eglinton, 2008). We put our new record into the context of those from regions further north and closer to Antarctica for an integrated reconstruction of Southern Ocean latitudinal SST gradients.

2 Material and methods

2.1 ODP Site 1168

Site 1168 (42°36.5809′ S, 144°24.7620′ E; 2463 m modern water depth; Fig. 1) is located on the continental slope of the western Tasmanian continental margin. The site sits on the northern edge of the Subtropical Convergence Zone, which separates warm, saline subtropical waters from comparably cold and fresh subantarctic water masses (Heath et al., 1985; Exon et al., 2001), with a modern SST ranging from 13–17 °C (winter–summer). During the Neogene, the location of Site 1168 tectonically drifted along with Tasmania and Australia from 52° S at 23 Ma to its modern position at 42° S (Van Hinsbergen et al., 2015). During this northward tectonic drift, the southern margin of Australia was continuously bathed by the eastward-flowing proto-Leeuwin Current (McGowran et al., 2004; Hoem et al., 2021). Hence, Site 1168 is well suited to the study of the Neogene evolution of the ACC and the STF.

2.2 Age model

The post-cruise bio-magnetostratigraphic age model includes nannofossil, planktonic foraminifer, diatom, radiolarian and dinocyst biostratigraphy, with constraints from magnetostratigraphy and stable isotope data (Stickley et al., 2004). Here, we recalibrated these data to the Geological Time Scale 2020 (Gradstein et al., 2020) by using state-of-the-art biostratigraphic constraints from Nannotax and Foramtax as well as updated diatom biostratigraphic constraints (Cody et al., 2008). We then fitted a loess smooth curve through these data, whereby we assigned a 10-fold weight to magnetostratigraphic and benthic $\delta^{18}O$ tie points. We interpolated this loess curve to obtain ages for the samples. We derive average sediment accumulation rates of 1.8 cm kyr^{-1} for the top 360 m (22–0 Ma) and 7.1 cm kyr^{-1} between 360 and 462 m below seafloor (m b.s.f.; 23–22 Ma; Fig. 2).

2.3 Lithology

A total of 883.5 m of sediment was recovered from Site1168 Hole A, dating back to the late Eocene to modern (Exon et al., 2001). The Neogene interval is represented in the upper 413 m. Between 260–413 m b.s.f. (early to mid-Miocene; 23.0–15.6 Ma), sediments are comprised of clay-bearing nannofossil chalk with a gradual decrease of non-carbonate minerals (Robert, 2004). The upper 260 m (mid-Miocene to modern; 15.6–0 Ma) contains calcareous biogenic oozes, with 85–97 wt % calcium carbonate (Exon et al., 2001); a sharp decrease in detrital clay content occurs at the boundary between these lithologic units (Robert, 2004).

2.4 Biomarker extraction and analysis

Lipid biomarkers were extracted from 433 powdered and freeze-dried samples with a Milestone ETHOS X microwave system using dichloromethane / methanol (DCM / MeOH) 9:1 (v/v). Activated Al_2O_3 columns were used for the separation of the total lipid extract into three fractions, using the solvent mixtures hexane / DCM 9 : 1 (v/v), hexane / DCM 1 : 1 (v/v) and DCM / MeOH 1 : 1 (v/v) for apolar, ketone and polar fractions, respectively. Polar fractions were filtered using a 0.45 µm polytetrafluorethylene filter and analysed us-

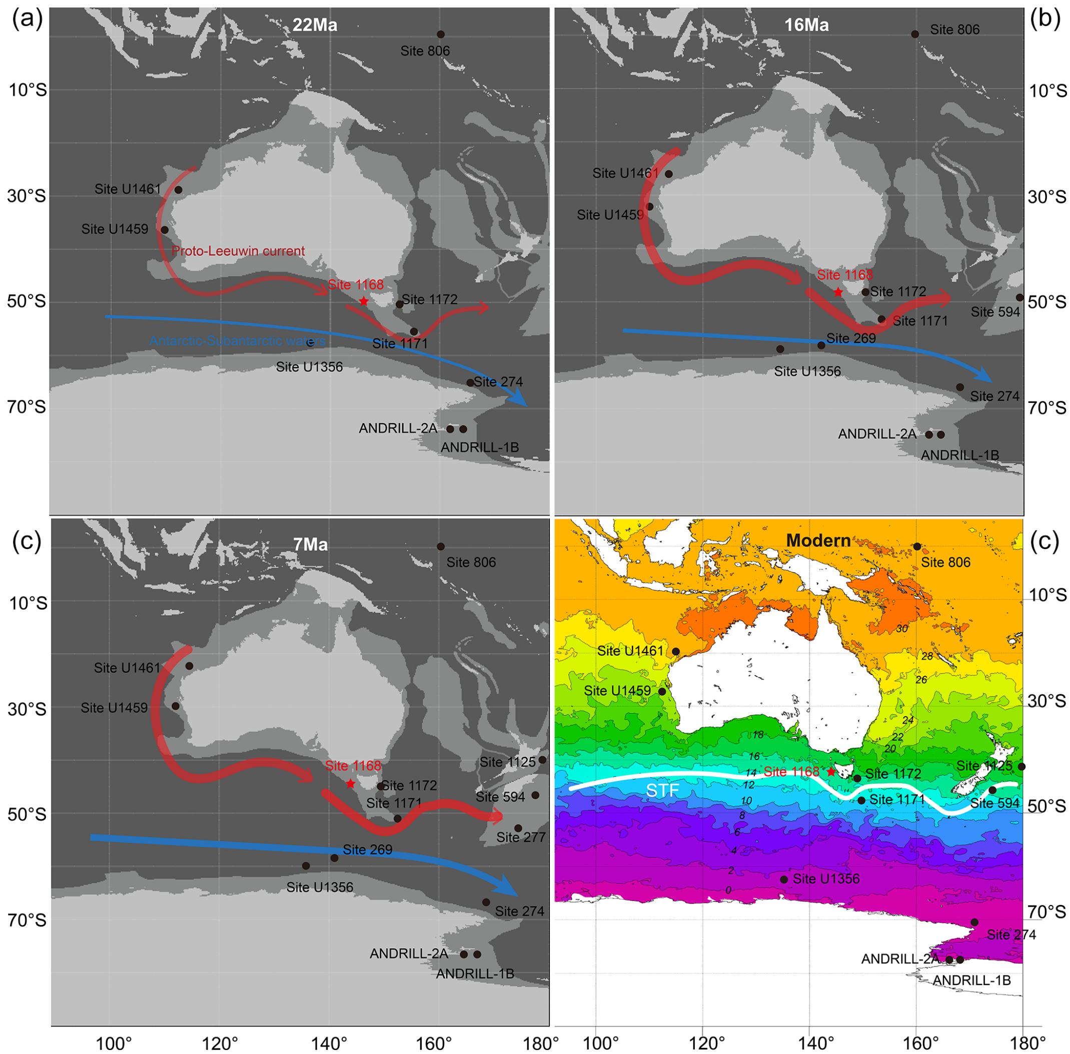

Figure 1. Neogene paleogeographic maps of the Australian–Antarctic sector, with the Deep Sea Drilling Program, Ocean Drilling Program and Integrated Ocean Drilling Program site locations referred to in this study. **(a, b, c)** Reconstructed map of studied area using GPlates (Torsvik et al., 2012; Van Hinsbergen et al., 2015) with inferred surface ocean currents (solid red and blue lines; De Vleeschouwer et al., 2019; Jackson et al., 2019; Sauermilch et al., 2021; Evangelinos et al., 2022). The thickness of the lines denotes the relative strength of the currents. The edge of the light-grey fill denotes present-day shorelines. The dark-grey contours indicate the edge of continental plates. Compiled sites and the site of this study are shown with black circles and a red star, respectively. **(d)** Modern map (modified from NOAA, https://www.ospo.noaa.gov/Products/ocean/sst/contour, last access: 13 March 2023) of the studied area filled with modern sea surface temperature, which is indicated by colours and contours and numbers on the contours. The white line indicates the subtropical front.

ing an Agilent 1260 Infinity series HPLC system coupled to an Agilent 6130 single quadrupole mass spectrometer, following the instrumental and analytical setup described in Hopmans et al. (2016). A total of 99 ng of C_{46} standard was added to the polar fraction in order to quantify the absolute concentration of GDGTs. The ketone fractions of 163 out of 433 samples were dissolved in ethyl acetate and analysed on a gas chromatograph (GC) coupled to a flame ionisation detector (GC-FID, Hewlett Packard 6890 series) equipped with a CP-Sil 5 fused-silica capillary column (25 m × 0.32 mm; film thickness 0.12 µm) and a 0.53 mm precolumn. Samples were injected on-column at 70 °C with helium as a carrier gas at a constant pressure of 100 kPa. The oven programme was as follows: 70 °C for 1 min, then it was ramped to 130 °C at 20 °C min^{-1}, then to 320 °C at 4 °C min^{-1}, and then it was held to be isothermal for 10 min. Di- and tri-unsaturated C_{37} alkenones were identified based on retention time. Data are stored at Zenodo (Bijl et al., 2022).

2.5 SST reconstruction and confounding-factor indices

We follow the approach by Sluijs et al. (2020) and Bijl et al. (2021) to assess non-temperature factors in relation to the relative distribution of isoGDGTs and thus the TEX_{86} value

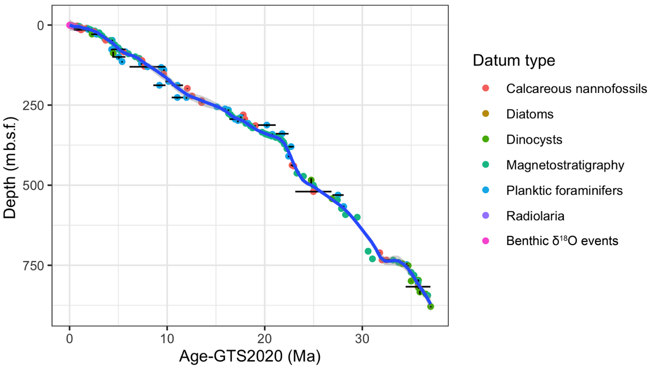

Figure 2. Age model of Site 1168. Points indicate the data (Stickley et al., 2004). Colours indicate data types. The blue curve indicates the loess smooth curve with a span of 0.1 throughout the studied interval, which we resampled to obtain ages for the samples used in this study.

they represent. Briefly, this involves checking the weighted average of cyclopentane moieties of isoGDGTs compared to modern values (with the Ring Index – RI; Zhang et al., 2016), overprints from methanotrophic archaea (with the Methane Index – MI; Zhang et al., 2011; Weijers et al., 2011) and methanogens (with the GDGT-0 / Cren ratio; Blaga et al., 2009), as well as contributions from deep-dwelling archaea (with the GDGT-2 / GDGT-3 ratio; Taylor et al., 2013) or terrestrial GDGTs (with the BIT index; Hopmans et al., 2004; Weijers et al., 2006). The BIT index is determined by the ratio of branched GDGTs (brGDGTs) produced by terrestrial bacteria and marine-originated crenarchaeol. However, recent studies have proved that brGDGTs can be produced in situ in marine environments (Peterse et al., 2009; Sinninghe Damsté, 2016; Dearing Crampton-Flood et al., 2019). Thus, the sources of brGDGTs are assessed using the weighted number of cyclopentane moieties in tetramethylated branched GDGTs (#rings$_{tetra}$), where a value of > 0.7 is assumed to indicate a marine rather than a terrestrial source of these compounds (Sinninghe Damsté, 2016). In order to assess the influence of potential algae distribution on the $U_{37}^{k'}$-based SST reconstruction, we explored the ratio between C_{37} and C_{38} (C_{37} / C_{38}; Rosell-Melé et al., 1994) and the ratio between all C_{37} and the ethyl C_{38} alkenones (C_{37} / C_{38Et}; Zheng et al., 2019).

Numerous calibrations have been implemented to translate TEX$_{86}$ into sea surface temperature (e.g. Schouten et al., 2002; Kim et al., 2010; Tierney and Tingley, 2014). However, improved understanding of archaea ecology questions the validity of TEX$_{86}$ as a true proxy for the ocean mixed-layer temperature. This is especially due to the variable export production zone depth (50–200 m) of marine Thaumarchaeota. Fortunately, this can be revealed by the GDGT-2 / GDGT-3 ratio, which suggests that many modern core top samples actually receive contributions from deep-dwelling archaea (Van der Weijst et al., 2022). Thus, the ambient temperature of Thaumarchaeota, which determines the cyclisation of GDGTs, is not strictly sea surface temperature. Even though the GDGTs may, to a variable extent, derive from around the thermocline, it was shown that SST has a strong relationship with surface temperature (Van der Weijst et al., 2022). Subsurface calibrations (Tierney and Tingley, 2014; Kim et al., 2015; Ho and Laepple, 2016) use variable methods to integrate temperature over depth; these methods still induce uncertainty with regard to their reliability. Nonetheless, even though a perfect calibration does not exist yet, TEX$_{86}$ is still a valuable proxy that reflects the temperature of a relatively stable layer of the ocean (e.g. Kim et al., 2016; Hurley et al., 2018) and provides a robust ocean temperature change in both trend and variability (Van der Weijst et al., 2022) because the relationship between the TEX$_{86}$ in sediments and surface temperature actually derives from the strong relationship between subsurface and surface temperature. In particular, when TEX$_{86}$ is used along with other temperature proxies (e.g. Super et al., 2020; Leutert et al., 2020), such as the one we use here ($U_{37}^{k'}$), both proxies together can provide better constrains on SST reconstructions.

Here, we apply the spatial linear Bayesian calibration BAYSPAR (Tierney and Tingley, 2014, 2015) to translate TEX$_{86}$ values into temperatures using both surface (0–20 m) and depth-integrated temperature (0–200 m) calibrations (prior mean of 20 °C; prior standard deviation of 20 °C). We applied the $U_{37}^{k'}$ paleothermometer based on alkenones as an independent additional paleothermometer. $U_{37}^{k'}$ index values were calculated following Prahl and Wakeham (1987) and were converted to SST using the BAYSPLINE calibration of Tierney and Tingley (2018) (prior standard deviation of 10 °C). We choose the Bayesian calibrations for both proxies for the consideration of both high-temperature applicability and spatial characteristics. These two proxies, together with the TEX$_{86}$-related overprint indices, are combined to determine the sea surface temperature (SST) change.

3 Results

3.1 GDGT-based temperature reconstruction

Our new GDGTs data are derived from 412.7 to 0 m b.s.f. (22.6–0 Ma). The concentrations of all GDGTs are consistently high ($\sim 50\,\mu g\,g^{-1}$ sediment for total isoGDGTs; see Fig. S1 in the Supplement) in the early Miocene and show a normal relative distribution, except for the interval around the MCO (287–256 m b.s.f.; Fig. S2). The isoGDGT concentration drops to $5\,\mu g\,g^{-1}$ sediment at the onset of the MCO and remains stable until 7 Ma. In the MCO interval, of all GDGTs, crenarchaeol (cren) and crenarchaeol (cren') decrease most strongly (to 1/400; GDGT-3 decreases to 1/200; GDGT-2 and GDGT-1 decrease to 1/100; GDGT-0 decreases to 1/25; Fig. S1). As cren is not in the TEX$_{86}$ index, its anomalous trends in abundance do not directly affect TEX$_{86}$ values but do affect the GDGT indices and ratios that have cren in the denominator. As a result of the extra decline in cren, GDGT-0 / cren, MI and GDGT-2 / cren all yield abnormally high values in the MCO interval (Fig. 3). The GDGT-2/3 ratio gradually increases from 5 to 8 throughout the record, with transient peaks in the early Miocene and MCO. Cut-off values for this ratio vary between 3 and 10 among users and sites (e.g. Leutert et al., 2020; Bijl et al., 2021; Van der Weijst et al., 2022). Hurley et al. (2018) demonstrated that the GDGT-2 / GDGT-3 values rapidly rise from 3–5 in the surface mixed layer (upper 150 m) to 20–25 at the thermocline depth (see also Basse et al., 2014; Hernández-Sánchez et al., 2014; Kim et al., 2016; Van der Weijst et al., 2022). In any case, sediments with GDGT-2 / GDGT-3 values > 3 might, to some extent, be biased towards deeper waters and thus to lower temperatures. The ΔRing Index varied from −2.2 to 1 in the whole record, and 152 data points fell outside the 95 % confidence interval of the RI-TEX_{86} array (Fig. S3).

BIT index values show a large range of variation, between 0.1 and 0.9, and show a prominent peak (∼ 0.9) during the MCO and consistent low values (∼ 0.1) in the Pliocene, indicating a potentially large contribution of GDGTs from land (Fig. 3). However, the $\#rings_{tetra}$ values are highly varied throughout time but are consistently elevated between 17 and 7 Ma, from 0.3 to more than 1.0, suggesting that brGDGTs have an in situ marine origin. In a ternary diagram of the tetra-, penta- and hexa-methylated brGDGTs, Site 1168 samples generally plot offset to the global soil cluster (Fig. S4), which also supports a non-soil origin. This would imply that the BIT index cannot be interpreted as an indicator of the input of terrestrial matter at this site.

TEX_{86} values of the early Miocene were around 0.65 but fluctuated, then they reached 0.8 at 16 Ma in the MCO interval, although these values are probably affected by non-thermal overprints. There is an abrupt decline in TEX_{86} values after the MCO and then a long-term decrease to 0.4 until 5 Ma. TEX_{86} values increased to 0.6 in the early Pliocene, then decreased to 0.36 at 1.35 Ma and eventually increased to 0.52 in the youngest sediment (Fig. 3). SSTs derived from the TEX_{86} are around 25 °C in the early Miocene section. TEX_{86} values at the peak MCO would equate to SSTs of 34 °C, followed by first a rapid cooling at around 14.5 Ma and then a more gradual down to 7 °C towards the end of the Miocene (Fig. 4). After an ephemeral warming to 20 °C in the early Pliocene, SST decreased to 6 °C in the mid-Pleistocene and then recovered to the modern level around 17 °C. Throughout the record, the difference between temperatures derived from surface and depth-integrated subsurface calibrations is small (< 2 °C).

3.2 Alkenone-based temperature reconstruction

Our new alkenone data are derived from 363 to 0 m b.s.f. (21.9–0 Ma). Existing $U^{k'}_{37}$ data from this site were published in Guitián and Stoll (2021). C_{38} alkenones are mostly at or below detection limit in the sediments older than 8 Ma. In the younger sediments, we find four clear peaks that represent C_{38} alkenones. Here, C_{37} / C_{38} fluctuates between 0.9 and 1.2, while C_{37} / C_{38Et} varies between 1.2 and 1.4 (Fig. S5). The $U^{k'}_{37}$ index record varies between 0.43 and 0.93 and generally follows the trends of TEX_{86}, except during the MCO and the early Pleistocene (Fig. 4). Early Miocene sediments have an average $U^{k'}_{37}$ value of ∼ 0.8, in agreement with previously published data from the same site (Guitián and Stoll, 2021). In the MCO interval, $U^{k'}_{37}$ rose to 0.93. None of the analysed sediments in the MCO interval have saturated $U^{k'}_{37}$ index values. Subsequently, $U^{k'}_{37}$ gradually drops to 0.43 at the end of the Miocene and recovers to ∼ 0.6 in the Pliocene. $U^{k'}_{37}$-based SSTs reveal similar temperatures to TEX_{86}-based subsurface temperature except in the MCO interval (Fig. 4). In the early Miocene, $SST_{U^{k'}_{37}}$ yields ∼ 24 °C on average, then increases to ∼ 28 °C in the MCO. Subsequently, $SST_{U^{k'}_{37}}$ cools down to 10 °C at 5 Ma and increases to 16 °C in the Pliocene. $SST_{U^{k'}_{37}}$ shows a similar trend to that of $SST_{TEX_{86}}$ in the Pleistocene and varies between 17 and 7.5 °C. However, the difference between $SST_{U^{k'}_{37}}$ and $SST_{TEX_{86}}$ increases from the onset of the Pleistocene due to the plunge of $SST_{TEX_{86}}$.

4 Discussion

4.1 Reliability assessment of the SST record

In all intervals of the records besides the MCO, temperature estimates derived from the $U^{k'}_{37}$ and TEX_{86} have similar trends and absolute temperatures, demonstrating that both proxies represent the same water layer. The large $U^{k'}_{37}$ / TEX_{86} discrepancy during the MCO suggests that one of the paleotemperature proxies is affected by non-thermal overprints (Figs. 4, 5). Given the many indices that signal anomalous isoGDGT distributions in the MCO interval, it is likely that TEX_{86} has a non-pelagic GDGT assemblage and thus reflects an unreliable SST. However, the high GDGT-0 / cren, MI, GDGT-2 / cren and BIT index values in the MCO interval are all caused by the anomalously low contribution of cren (i.e. the denominator) and not that of the elevated relative abundances of the signalling compound for that overprint (the nominator). Moreover, the low total organic carbon (TOC) wt % (< 0.5 %; Exon et al., 2001) in the MCO sediments does not support the existence of any cold seeps, anaerobic oxidation of methane or methane hydrate production despite the high GDGT-0 / cren, MI and GDGT-2 / cren values (Fig. 3). If it is indeed the excess relative decrease in cren concentration that causes the high BIT, GDGT-0 / cren, MI and GDGT-2 / cren and the low RI because all have cren involved in their equation – the question is to what extent this affects TEX_{86} values. In any case, the indices may not necessarily reflect the overprints that they are usually associated with at this site. However, since TEX_{86} and $U^{k'}_{37}$ disagree in the same interval as the anomalous GDGT compositions, and

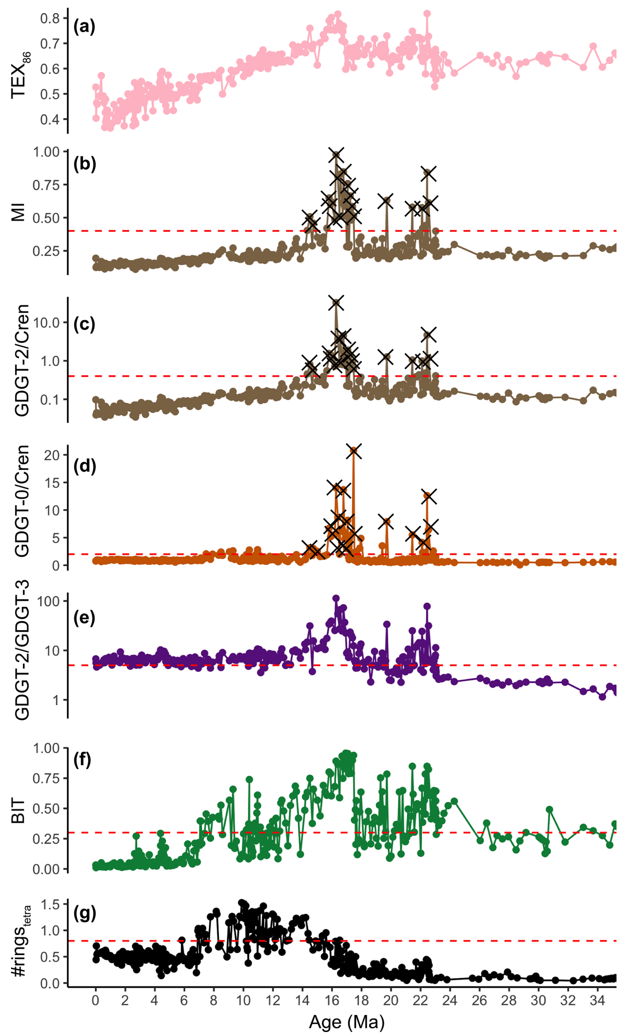

Figure 3. TEX_{86} values and indices and ratios to detect non-thermal GDGT contributions. Dashed red lines indicate proposed threshold values. **(a)** TEX_{86}. **(b)** Methane index, threshold = 0.4 (Zhang et al., 2011). **(c)** GDGT-2 / cren, threshold = 0.4 (Weijers et al., 2011). **(d)** GDGT-0 / cren, threshold = 2 (Blaga et al., 2009). **(f)** BIT, usually applied threshold = 0.3 (Hopmans et al., 2004). **(e)** GDGT-2 / GDGT-3, threshold = 5 (Taylor et al., 2013). **(g)** $\#rings_{tetra}$, threshold = 0.8 (Sinninghe Damsté, 2016). Discarded data are shown by crosses.

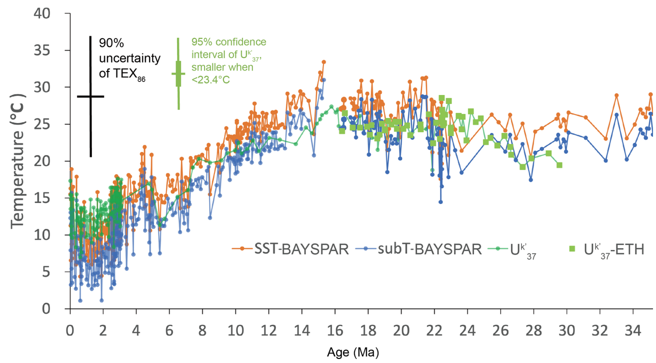

Figure 4. TEX_{86} and $U^{k'}_{37}$ SST reconstructions of Site 1168. The BAYSPAR calibration (Tierney and Tingley, 2014) is used to translate TEX_{86} values into surface (orange points) and subsurface (blue points) temperatures. $U^{k'}_{37}$ SST reconstruction (dark green) based on the BAYSPLINE calibration (Tierney and Tingley, 2018). All new data are denoted by dots. Oligocene–early Miocene $U^{k'}_{37}$ SSTs of Guitián and Stoll (2021) are represented by green squares.

to be conservative, we discard the TEX_{86}-based SSTs with high confounding-factor values in the MCO interval at this site.

The anomalously low relative abundance of cren could be explained by different preservation efficiency and/or degradation rates for distinct GDGTs. The interval in which GDGT concentrations decrease (17.34–16.85 Ma, 294.66–274.28 m b.s.f.) is concomitant to an interval of decreased terrigenous clay and quartz and increased calcium carbonate content (Fig. 5; Robert, 2004). The loss of terrigenous clay can lead to reduced preservation of organic matter (Ransom et al., 1998; Wu et al., 2019) because enhanced porewater flow in the overlying sediment enhances oxygen exposure time (Huguet et al., 2008; Schouten et al., 2013). It was shown that isoGDGTs with more cyclopentane moieties are less resistant to oxidation than those with less cyclopentanes (Ding et al., 2013). As a result, degradation processes would result in lower TEX_{86} values and an underestimation of SSTs. However, in the MCO interval, TEX_{86} was very high and led to SST reconstructions that were much higher than SST_{UK37}. While selective degradation could be an explanation for the relatively excessive loss of cren, it cannot explain the anomalously high TEX_{86}-based SSTs in that interval. On the other hand, preferential degradation of alkenones could have biased $U^{k'}_{37}$ at this site as well, notably in the form of a warm bias in SST (Freitas et al., 2017). Yet, in the MCO interval, we do not observe anomalous warmth, and the index is not yet saturated. Therefore, the selective degradation in alkenones cannot explain the SST difference between SSTs derived from $U^{k\prime}_{37}$ and TEX_{86}.

The extremely high (up to 100) GDGT-2 / GDGT-3 ratio found in the MCO is unprecedented in both paleo and modern ocean records (e.g. Taylor et al., 2013; Hernández-Sánchez et al., 2014; Hurley et al., 2018; Besseling et al., 2019; Bijl et al., 2021; Van der Weijst et al., 2022). Perhaps the isoGDGTs found in the MCO interval were produced by other archaeal communities, e.g. Marine Group II and/or III (Besseling et al., 2019), and the ratio could have been further increased through selective degradation of GDGT-3 over GDGT-2. Given the temperature trend in the MCO interval, these GDGT producers may have also responded to water temperature, although indirectly or with a different dependency. In the early and late Miocene, GDGT-2 / GDGT-3 values are still relatively high (> 5), indicating some isoGDGT input from deep-water sources. The overall input of deeper-dwelling GDGTs may bias the reconstruction of absolute SSTs from TEX_{86}, but because the GDGT2/3 ratio in our post-MMCT interval is stable and without a trend, the trend of TEX_{86} should not be influenced (Ho and Laepple, 2016; Leutert et al., 2020; Van der Weijst et al., 2022), and the amplitude is well constrained by $U^{k'}_{37}$. Thus, for the late Miocene and Pliocene, the sediments are not discarded despite high GDGT-2 / GDGT-3 values. Despite nearly half of the data points falling out of the 95 % confidence interval of the TEX_{86} Ring Index, we decided to not discard those because most of the sediments with abnormal Ring Index values are caused by the highly reduced contribution of cren.

C_{37} / C_{38} and C_{37} / C_{38Et} ratios do not show any profound change; thus, we infer that alkenone composition is not affected by algae composition changes, and thus, $U^{k'}_{37}$ represents sea surface temperature. While TEX_{86}-derived SST is in a consistently similar range or above $U^{k'}_{37}$-derived SST throughout most of the record, with the onset of the Pleistocene, $SST_{TEX_{86}}$ drops significantly when compared to SSTs derived from alkenones. However, the difference is around 3 °C, which is still within the calibration errors. Nevertheless, such difference is mainly due to the use of BAYSPAR calibration. SST results using BAYSPAR calibration are barely different from TEX^H_{86} based on the temperature output when $TEX_{86} > 0.5$. However, when TEX_{86} is smaller than 0.5, namely in the Pleistocene, TEX^H_{86}-based SST is well in line with $SST_{U^{k'}_{37}}$ (Fig. S6).

Overall, considering the small difference (∼ 2 °C) between surface and subsurface calibration of TEX_{86} and $SST_{U^{k'}_{37}}$, the relatively large calibration error of proxies, and the similar extent of variability and the high GDGT-2 / GDGT-3 ratio throughout the study interval, we deem it that both proxies mainly reflect temperature of the surface layer, with TEX_{86} integrating a deeper component. Hence, we claim that our temperature record is a sea surface temperature (SST). However, we focus on the $U^{k'}_{37}$ record when we interpret the record during the MCO.

4.2 Site1168 SST evolution and Southern Ocean temperature gradient in the Neogene

The new SST record for Site 1168 shows in broad lines a similar trend to that of the global compilation of the benthic foraminiferal oxygen isotope stack ($\delta^{18}O_{bf}$); however, there are some interesting deviations (Fig. 6). The mid-to-late Miocene interval contains a remarkable ∼ 10 °C gradual SST cooling that is much less prominent in $\delta^{18}O_{bf}$ (Fig. 6). Other than the late Miocene cooling, we have found that subtropical SSTs fluctuated around 26 °C in the early Miocene, which is similar to those in the Oligocene (Fig. 4; Guitián and Stoll, 2021; Hoem et al., 2022). The SST record from > 23 Ma is elaborately discussed in Hoem et al. (2022), so we will focus on the SST trends in the interval < 23 Ma. SSTs were slightly elevated in the MCO and rapidly cooled by 5 °C across the MMCT. Pliocene and Pleistocene SSTs at Site 1168 have larger variability than those in the late Miocene. However, the variability remains in the Pliocene and Pleistocene, which deviates from the $\delta^{18}O_{bf}$ feature.

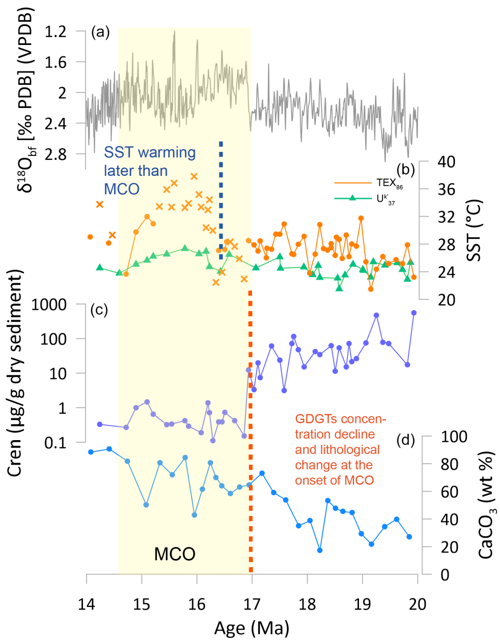

Figure 5. Lithology, GDGT concentrations and relative distributions and SST changes in the mid-Miocene. **(a)** Benthic foraminiferal $\delta^{18}O$ compilation (Westerhold et al., 2020). **(b)** SST changes based on TEX_{86} and $U^{k'}_{37}$ (this study; Guitián and Stoll, 2021). Orange dots indicate data points that are considered to be reliable, and crosses indicate data points of TEX_{86} that are considered to be unreliable. **(c)** The absolute abundance of cren as an indicator of GDGT preservation. **(d)** Weight % calcium carbonate indicating lithology change, inversely related to clay content (Robert, 2004). The dashed orange line indicates the change of lithology while isoGDGT preservation changes occur at the onset of MCO. The dashed blue line indicates the SST warming, postdating the MCO. The yellow bar indicates the interval of MCO.

The northward movement of the site, from ∼ 52° S in the early Miocene to ∼ 42° S at present, may have dampened the amplitude of Neogene long-term cooling to an unknown extent. However, during the Oligocene, ocean conditions at this site also barely changed despite the northward drift, likely because the ocean currents migrated northwards along with the tectonic drift of Australia (Hoem et al., 2021). Similarly, for the same reason, the northward tectonic drift of Australia during the Neogene, in other words the latitude change, may have had little effect on the temperature evolution at this site, thus records the temperature resulting in both global climate and water mass change at Site 1168. The synchronous tectonic drift of other mid-latitude sites warrants the conclusion about the latitudinal temperature gradient drawn from the comparison (Fig. 6a). With the consistency of both paleotemperature proxy results in consideration, we will further

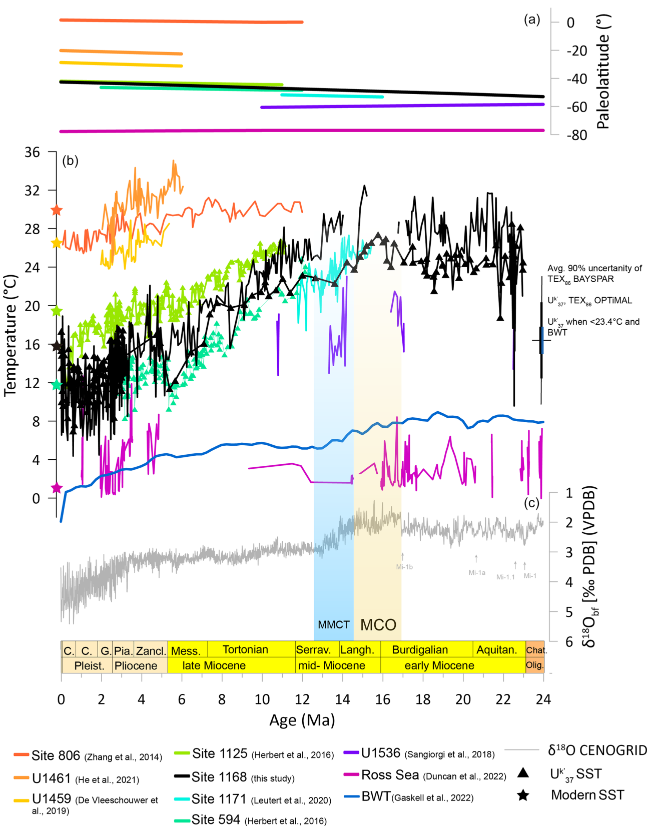

Figure 6. (a) Paleolatitude reconstruction using GPlates (Torsvik et al., 2012; Van Hinsbergen et al., 2015) of Site 1168 (this study; Guitián and Stoll, 2021), Site 806 (Zhang et al., 2014), Site U1461 (He et al., 2021), Site 1171 (Leutert et al., 2020), Site U1459 (De Vleeschouwer et al., 2019), Site 594, Site 1125 (Herbert et al., 2016), Site U1356 (Hartman et al., 2018; Sangiorgi et al., 2018) and the Ross Sea compilation (AND-1B, AND-2A, DSDP 274, DSDP 270, CIROS 1, CRP 2/2A; McKay et al., 2012; Levy et al., 2016; Sangiorgi, 2020; Duncan et al., 2022). **(b)** Reconstructed SST of the same sites using BAYSPAR and OPTiMAL (Ross Sea only) calibrations for TEX_{86} (no symbol) and BAYSPLINE for $U^{k'}_{37}$ (triangles) and bottom-water temperature based on benthic foraminiferal $\delta^{18}O$ (Gaskell et al., 2022). **(c)** Benthic foraminiferal $\delta^{18}O$ compilation (Westerhold et al., 2020). Modern SSTs of the sites are indicated by the coloured stars at 0 Ma.

discuss the SST evolution per time interval, focusing on variability within the record, comparison to the $\delta^{18}O_{bf}$ as a representation of deep-sea temperature and global ice volume trends, and comparison to other SST records in the region to reconstruct latitudinal SST gradients.

4.2.1 Early Miocene (23.04–17.0 Ma)

In the early Miocene, SST was around 26 °C but was punctuated by several short cooling events (Fig. 6). SST minima occurred at 22.4, 19.5 and 17 Ma, roughly time-equivalent to ephemeral positive excursion events (Mi-1.1, Mi-1a, Mi-1b) in $\delta^{18}O_{bf}$ (Miller et al., 1991; Billups et al., 2002; Liebrand et al., 2011; Westerhold et al., 2020). SSTs from the Wilkes Land margin (U1356) reflect similar events at 22.4 and 17 Ma (Sangiorgi et al., 2018; Hartman et al., 2018). In contrast, SSTs in the Ross Sea remained relatively stable and profoundly cooler than U1356, around 4 °C using the OPTiMAL calibration (Duncan et al., 2022). We choose OPTiMAL as the calibration for the Ross Sea sites because the Ross Sea experienced glacial phases in the early and middle Miocene (Passchier et al., 2011; Marschalek et al., 2021), while the Wilkes Land margin continued to be surrounded by warm oligotrophic waters (Bijl et al., 2018; Sangiorgi et al., 2018).

The latitudinal SST gradient between the STF and the higher latitudes was relatively constant during the early Miocene, remaining around 9 °C (Fig. 7). This gradient is very similar to the modern gradient between 51° S and the Antarctic margin (10 °C; Figs. 1, 7; Hartman et al., 2018) and represents a similar gradient to that of the late Oligocene (Hoem et al., 2022). Such a gradient may testify to the presence of a relatively strong proto-ACC when the Tasmanian Gateway aligned to the westerly winds (Pfuhl et al., 2004; Scher et al., 2015; Sauermilch et al., 2021), although the absolute SSTs at both sites were higher in the Miocene than today (Fig. 6).

A recent study (Kim and Zhang, 2022) suggested that a massive methane hydrate destabilisation event took place at the southern Australian margin during the Oligocene–Miocene boundary based on an elevated MI and more negative compound-specific carbon isotopes of Site 1168. However, based on the age model of Stickley et al. (2004) calibrated to GTS 2020, the Oligocene–Miocene boundary indicated by Kim and Zhang (2022) at ∼416 m b.s.f. is actually around 22.6 Ma. On the other hand, the high MI is actually induced by less cren and more GDGT-0 rather than by an increase in GDGT-1,2,3 (Fig. S1), which are thought to be produced by methanotrophic archaea. Thus, we doubt whether the evidence is concrete enough to prove a major methane hydrates dissociation in the early Miocene, but we acknowledge their hypothesis.

4.2.2 MCO (17.0–14.5 Ma)

SST_{UK37} shows a slight warming of ∼2 to ∼27 °C at the onset of the MCO (Figs. 5, 6). As this warming cannot be ascribed to saturation of the proxy, this would mean that the SST increase during the MCO is indeed smaller at the STF than at high-latitude sites and than what would be assumed from the strong change in $\delta^{18}O_{bf}$ at this time. Still, also at Site 1168, the mid-Miocene stands out as a warm time interval, consistent with other records, both surface and bottom (Levy et al., 2016; Sangiorgi et al., 2018; Modestou et al., 2020). Compared to the clear trends in the global $\delta^{18}O_{bf}$ record (Westerhold et al., 2020), the onset of the MCO is less clearly expressed in the records of SST (this study, Shevenell et al., 2004; Levy et al., 2016; Hartman et al., 2018; Super et al., 2018, 2020) and of Mg / Ca-based bottom-water temperature (Lear et al., 2015). Hence, the relationships between changes in surface oceanography, ice volume and deep-sea temperature at the MCO onset remain unresolved at this stage. In addition, the currently available clumped isotope records do not fully capture the 16–17 Ma interval (Modestou et al., 2020; Meckler et al., 2022), which makes disentangling ice volume and deep-sea temperature effects in $\delta^{18}O_{bf}$ at the MCO onset problematic.

The lithological change of Site 1168 at the onset of the MCO coincides with the biomarker preservation change but precedes regional warming and $\delta^{18}O_{bf}$ decline (Fig. 5). The increase of calcium carbonate indicates a change in the depositional setting, likely due to an intensification of the proto-Leeuwin Current (PLC). The intensification of the PLC during MCO is interpreted from deepest-seabed scouring (Jackson et al., 2019). The reported existence of larger foraminifera (Gouley and Gallagher, 2004) and, perhaps, although debated, tropical corals (McGowran et al., 1997) in the Great Australian Bight (Fig. 1) is likely related to the warm water induced by the PLC. Besides the increase of surface calcite productivity, this led to better-ventilated bottom water and warm oligotrophic surface water conditions during MCO. The potentially limited preservation of GDGTs may be related to improved bottom-water oxygenation (Huguet et al., 2008).

The SST records from Site 1168, near the subtropical front, and Site 1171, in the subantarctic zone, suggest that the latitudinal SST gradient collapsed to 0 (Fig. 7). This implies that the latitudinal SST gradient across the Tasmanian Gateway was strongly reduced in the MCO. The reduced latitudinal temperature gradient persisted both equatorward and poleward. Similarly, in the eastern equatorial Pacific (Rousselle et al., 2013), the latitudinal SST difference between the Equator and subtropical region was reduced to $\sim 2\,°C$. We also note that the SSTs of Site 1168 and of high-latitude sites (Wilkes Land, Ross Sea) are close to each other (Fig. 7), even though SST reconstructions of high-latitude sites are sparse (U1356) and absolute values are highly dependent on the used calibration (Ross Sea sites; Fig. 6). The reduced latitudinal SST gradient between mid-latitude and polar regions (Figs. 6, 7) agrees with certain modelled results for the MCO (Herold et al., 2011, 2012) but is not captured by other modelling (Burls et al., 2021). The weakened latitudinal SST gradient means that the ACC and associated fronts were weaker and/or located closer to Antarctica. Meanwhile, enhanced evaporation led to more precipitation in the high latitudes, at least on the Antarctic continental margin (Sangiorgi et al., 2018). The global heat transport also likely weakened with latitudinally more equable latitudinal climates (Chiang, 2009).

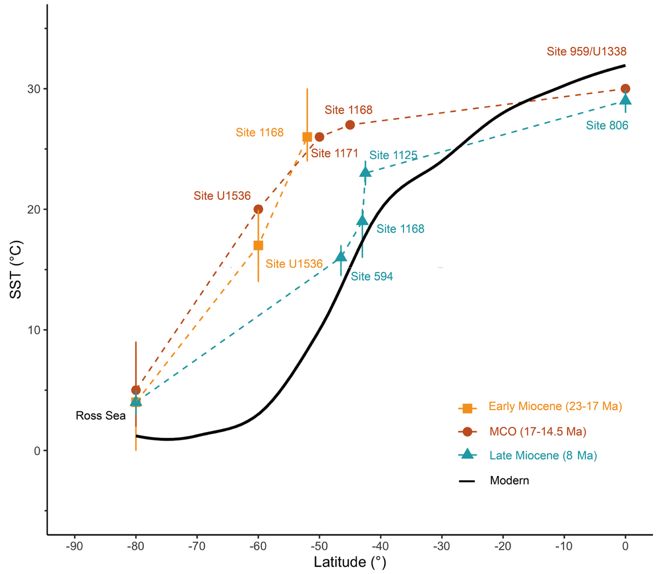

Figure 7. Sea surface latitudinal temperature gradient in the Southern Hemisphere for the early Miocene (orange; 23–17 Ma), MCO (red; 17–14.5 Ma), late Miocene (blue; 8 Ma) and modern at 160° E (black; based on Fig. 1d), respectively. Error bars indicate the variability of the time range. Paleo data are from the sources in Fig. 6, except for the MCO SSTs at the Equator, which are from Rousselle et al. (2013) and Van der Weijst et al. (2022).

4.2.3 MMCT (14.5–12.5 Ma)

The termination of the MCO is reflected by a sharp 5 °C decrease in SST at Site 1168 from 14.5 to 13 Ma, coincident with the time of cooling at the nearby Site 1171 (Leutert et al., 2020) (Fig. 6). This cooling phase coincided with a strong increase in $\delta^{18}O_{bf}$, which mostly reflects Antarctic ice sheet expansion (Shevenell et al., 2004, 2008; Leutert et al., 2020) and potential northward expansion of subantarctic waters (Leutert et al., 2020) accompanied by pCO_2 decline (Super et al., 2018). The SST gradient between the middle (Site 1168 and Site 1171) and high latitudes (Site U1356) increased, suggesting stronger fronts with amplified cooling towards Antarctica (Fig. 6). This is most likely a result of polar amplification of cooling towards high latitudes, further exacerbated by the expanding ice sheet and northward migration of frontal systems.

4.2.4 Late Miocene (12.5–5.3 Ma)

After the MMCT, SSTs at Site 1168 gradually cooled by 10 °C from 13 to 5 Ma, and the short-term variability amplitude was notably small (2–3 °C;Fig. 6). The amplitude of this cooling is comparable to that at other mid-latitude sites, i.e. Site 594 and Site 1125 in the southwest Pacific (Herbert et al., 2016).

The absolute temperatures and the cooling trend in the SST record of Site 594 seem to be in agreement with those at

Site 1171, which is located at the same latitude and is bathed by the same subantarctic water in the modern system. Thus, we can consider Site 1171 and Site 594 to be one continuous record representing the ocean temperature 5° S of Site 1168. Furthermore, the temperature difference between closely located subtropical (Site 1125 and Site 1168) and subantarctic (Site 594 and Site 1171) sites became larger by about 4 °C between each area (Figs. 6, 7). We deduce from this that the STF progressively got stronger. The Equator–mid-latitude temperature gradient also progressively increased (Fig. 7). Equatorial SST of Site 806 in the western Pacific decreased by only 3 °C from 12 to 5 Ma (Zhang et al., 2014). Given the low temperatures at the high latitudes by the end of the Miocene (Gaskell et al., 2022; Fig. 6), the Southern Ocean Equator-to-pole latitudinal temperature gradient and the SSTs of the studied sites must have been very similar (~ 26 °C) to modern conditions. Notably, the relatively strong Southern Ocean cooling trend is not reflected in the $\delta^{18}O_{bf}$ record, which remained relatively stable over this time interval. Thus, the relationship between Southern Ocean cooling, deep-sea temperature change and ice volume change still needs further study for this interval.

The increased SST gradient reflects a combination of global cooling and the amplification effect of northward migration of the STF, which effectively extends the Southern Ocean over wider latitudes. This change in temperature gradient between equatorial sites and Site 1168 also indicates a weakening of the Leeuwin Current (De Vleeschouwer et al., 2019). The gradually increased Equator in relation to high mid-latitude SST gradients led to a contracted and strengthened Hadley cell, which consequently caused an aridification in subtropical regions by intensifying the evaporation in the descending limb (Herbert et al., 2016; Groeneveld et al., 2017). This is reflected at Site 1168 and at other Tasmanian sites with an increase in the contribution of kaolinite and/or illite, reflecting the erosion of old soils as a result of aridification of the hinterland and subsequent transport by the westerlies since the late Miocene (since ~ 200 m b.s.f. of Site 1168; Robert, 2004).

During 8–5.3 Ma, several stepwise changes occur in the Southern Ocean. Tanner et al. (2020) indicated a northward STF shift at the Agulhas ridge from 8 Ma onwards, while Groeneveld et al. (2017) suggested a southward migration of the westerlies near southwest Australia in the same period. This apparent discrepancy can be partly accounted for with the northward tectonic movement of Australia while the STF remained at its position or moved northward at a slower pace than the continent (De Vleeschouwer et al., 2019), while the Agulhas plateau experienced limited tectonic movement. This would mean that Site 1168 entered the subtropical zone and received more warm subtropical water through the Leeuwin Current, therefore reducing the temperature difference between western Australian coastal sites. However, the increased SST difference that we observe between Site 1168 and northwest Australia and the Equator (Fig. 6) suggests a weaker PLC and thus does not seem to support this interpretation. Another explanation for the discrepancy between Tanner et al. (2020) and Groeneveld et al. (2017) is that the STF did not necessarily align to the position of the westerlies (De Boer et al., 2013). The relative positional shift between the Australian continent and the westerlies does not directly influence the position of the STF when the STF remains bound by the southern edge of the Australian continent during this time. Christensen et al. (2021) suggests that changes in the Tasman leakage around 7 Ma may have an influence on the global circulation in accordance with a southward migration of the westerlies. However, the Tasman leakage represents an intermediate water layer (400–900 m) which would not necessarily have influenced SST. Indeed, the SST record does not show a prominent, step-wise change around the time of the onset of the Tasman leakage.

4.2.5 Pliocene to modern (5.3–0 Ma)

Following late Miocene cooling from its minimum in the latest Miocene (Herbert et al., 2016), the Pliocene SSTs of Site 1168 shifted back to generally warm conditions (16 °C; Fig. 6). Compared to the modest variability in $\delta^{18}O_{bf}$ in the Pliocene, SST change at the STF is relatively large in amplitude (8 °C). The early Pliocene warmth found at site 1168 coincides with the SST record of the northwest Australian continental shelf (He et al., 2021), thus confirming the existence of a relatively strong Leeuwin Current which causes the SST rise. The subsequent cooling after 4 Ma until the mid-Pleistocene led to an increased SST gradient between Site 1168 and the western Australian coast sites along the Leeuwin Current pathway, therefore indicating a stepwise weakening (De Vleeschouwer et al., 2019; Fig. 6). The Pliocene SST variability at Site 1168 may be amplified by the combined effects of a changing Leeuwin Current, migrating STF and strong ice sheet fluctuations in Antarctica, and the variability would then be stronger than during the Miocene. SST shifts can be roughly correlated to known $\delta^{18}O_{bf}$ events, such as the mid-Piacenzian Warm Period and M2 glaciation. Intriguingly, in the Pliocene–Pleistocene interval, the SST of Site 1168 varied synchronously with that in the Ross Sea, which lead to a constant temperature gradient of ~ 8 °C between middle and high latitudes.

In summary, the Neogene SST record of the STF is characterised by five phases of accelerated cooling of ~ 2–3° at ~ 14, 9, 7, 5.5 and 2.8 Ma, superimposed on the gradual cooling trend (Fig. 6). Overall, by comparing our mid-latitude SST record with other sites in the Southern Hemisphere, we show that the latitudinal gradient of the Southern Ocean varied from weak (23–17 Ma), to weakened (17–14.5 Ma), to strengthening (14.5–5 Ma), to variable (5–0 Ma; Fig. 7), which we link to the gradual development of the frontal systems in the Southern Ocean, related to the interplay between the ice sheet, tectonic and climatic evolution of the Neogene Southern Ocean. The long-term evolution of subtropical-front SSTs is consistent with that of $\delta^{18}O_{bf}$, except for the progressive 10 °C cooling in the late Miocene that is less pronounced in $\delta^{18}O_{bf}$ (∼ 0.3 ‰; Fig. 6). Perhaps this reflects a nonlinear response of subtropical-front SSTs to the progressive buildup of ice sheets once it has passed a critical threshold, including that of the western Antarctic ice sheet (Marschalek et al., 2021), and a more persistent presence of sea ice (Sangiorgi et al., 2018). In general, we observe modest cooling in the equatorial Pacific region throughout the Neogene and also modest cooling at the Antarctic continental margin. However, the strong cooling in the subtropical-front region suggests that the shape of the meridional temperature gradient changed fundamentally, with a broad, warm Southern Ocean in the mid-Miocene and a progressive expansion of cold-temperate conditions towards lower latitudes thereafter. This could be caused by a progressive increase in the strength of the ACC, strengthening latitudinal SST gradients in middle to low latitudes. Further study should reveal the exact changes of both surface oceanographic conditions (not exclusively SST but also upwelling and salinity) and deep-water temperature (including separate deep-water temperature and ice volume signals).

5 Conclusion

Our Neogene SST record from offshore Tasmania, derived from two independent biomarker proxies, provides for the first time a continuous, long-term record of subtropical Southern Ocean SST evolution during the Tasmanian Gateway opening. The SST record reflects a warm mid-Miocene climatic optimum, a gradual but profound 10 °C cooling in the mid-to-late Miocene, renewed warming in the Pliocene and highly variable temperature conditions during the Pleistocene to modern times. The long-term SST trend is consistent with the $\delta^{18}O_{bf}$ record, except during the late Miocene cooling. Short-term SST variability in the record can be linked to glacial–interglacial phases, suggesting strong coupling between Antarctic ice sheet buildup and the subtropical-front temperature on a multi-million-year timescale. However, the mechanism of the decoupling between SST and $\delta^{18}O_{bf}$ during the late Miocene is still enigmatic. Comparison with previously published SST records indicates that the latitudinal gradient in the Southern Ocean experienced a stepwise development, from a relatively strong gradient in the early Miocene to reduced gradients during the MCO to a steepening during the mid-to-late Miocene. Pliocene to modern time gradients remain relatively constant in trend but may differ in range over glacial–interglacial cycles. During the late Miocene cooling, the latitudinal SST gradient between the STF and the Pacific Equator profoundly increased (from 4 to 14 °C), while the SST gradient between the STF and the Antarctic margin decreased due to amplified STF cooling and relatively stable near-Antarctic SSTs. This caused a progressive narrowing of the warm equatorial-to-subtropical heat distribution and an expansion of subpolar conditions to lower latitudes. Our study presents a continuous picture of the STF temperature evolution in the Southern Ocean Tasmanian Gateway area and reveals the history of frontal systems towards modern conditions.

Data availability. The TEX_{86} and $U^{k'}_{37}$ data of ODP Site 1168 are deposited at Zenodo https://doi.org/10.5281/zenodo.7119904 (Bijl et al., 2022).

Supplement. The supplement related to this article is available online at: https://doi.org/10.5194/cp-19-787-2023-supplement.

Author contributions. PKB designed the research. SH, FH and FL processed samples for organic geochemistry (TEX_{86} and $U^{k'}_{37}$). All authors contributed to analysing the data. SH designed the figures and wrote the paper with input from FS, FP and PKB.

Competing interests. The contact author has declared that none of the authors has any competing interests.

Disclaimer. Publisher's note: Copernicus Publications remains neutral with regard to jurisdictional claims in published maps and institutional affiliations.

Acknowledgements. We thank Mariska Hoorweg, Klaas Nierop, Desmond Eefting and Addison Rice for the laboratory assistance. We thank Johan Weijers, Benjamin Petrick, Guodong Jia, Stefan Schouten, Robert McKay and Bella Duncan for providing the corresponding data which were used to interpret the results. We thank IODP and the shipboard scientists of ODP 189, especially KCC in Japan, for the help with sampling. Additional gratitude is sent to Kun Huang for helping generate Monte Carlo simulations of GDGT compositions, although not included in the paper, and Mei Nelissen for the preliminary data analysis. We thank the reviewers, Igor Obreht and Benjamin Petrick, for their constructive comments that helped improve our paper.

Financial support. This research has been supported by the European Research Council, H2020 European Research Council (OceaNice (grant no. 802835)).

Review statement. This paper was edited by Bjørg Risebrobakken and reviewed by Igor Obreht and Benjamin Petrick.

References

Basse, A., Zhu, C., Versteegh, G. J. M., Fischer, G., Hinrichs, K. U., and Mollenhauer, G.: Distribution of intact and core tetraether lipids in water column profiles of suspended particulate matter off Cape Blanc, NW Africa, Org. Geochem., 72, 1–13, https://doi.org/10.1016/j.orggeochem.2014.04.007, 2014.

Besseling, M. A., Hopmans, E. C., Koenen, M., van der Meer, M. T. J., Vreugdenhil, S., Schouten, S., Sinninghe Damsté, J. S., and Villanueva, L.: Depth-related differences in archaeal populations impact the isoprenoid tetraether lipid composition of the Mediterranean Sea water column, Org. Geochem., 135, 16–31, https://doi.org/10.1016/j.orggeochem.2019.06.008, 2019.

Bijl, P. K., Houben, A. J. P., Hartman, J. D., Pross, J., Salabarnada, A., Escutia, C., and Sangiorgi, F.: Paleoceanography and ice sheet variability offshore Wilkes Land, Antarctica – Part 2: Insights from Oligocene–Miocene dinoflagellate cyst assemblages, Clim. Past, 14, 1015–1033, https://doi.org/10.5194/cp-14-1015-2018, 2018.

Bijl, P. K., Frieling, J., Cramwinckel, M. J., Boschman, C., Sluijs, A., and Peterse, F.: Maastrichtian–Rupelian paleoclimates in the southwest Pacific – a critical re-evaluation of biomarker paleothermometry and dinoflagellate cyst paleoecology at Ocean Drilling Program Site 1172, Clim. Past, 17, 2393–2425, https://doi.org/10.5194/cp-17-2393-2021, 2021.

Bijl, P. K., Hoem, F. S., and Hou, S.: sea-surface temperature proxy data (TEX_{86} and UK'_{37}) from Ocean Drilling Program Site 1168, Zenodo [data set], https://doi.org/10.5281/zenodo.7119904, 2022.

Billups, K., Channell, J. E. T., and Zachos, J.: Late Oligocene to early Miocene geochronology and paleoceanography from the subantarctic South Atlantic, Paleoceanography, 17, 4-1–4-11, https://doi.org/10.1029/2000pa000568, 2002.

Blaga, C. I., Reichart, G. J., Heiri, O., and Sinninghe Damsté, J. S.: Tetraether membrane lipid distributions in water-column particulate matter and sediments: A study of 47 European lakes along a north-south transect. J. Paleolimnol., 41, 523–540, https://doi.org/10.1007/s10933-008-9242-2, 2009.

Burls, N. J., Bradshaw, C. D., De Boer, A. M., Herold, N., Huber, M., Pound, M., Donnadieu, Y., Farnsworth, A., Frigola, A., Gasson, E., von der Heydt, A. S., Hutchinson, D. K., Knorr, G., Lawrence, K. T., Lear, C. H., Li, X., Lohmann, G., Lunt, D. J., Marzocchi, A., Prange, M., Riihimaki, C. A., Sarr, A. -C., Siler, N., and Zhang, Z.: Simulating Miocene Warmth: Insights From an Opportunistic Multi-Model Ensemble (MioMIP1), Paleoceanography and Paleoclimatology, 36, e2020PA004054, https://doi.org/10.1029/2020PA004054, 2021.

Chiang, J. C.: The tropics in paleoclimate, Annu. Rev. Earth Pl. Sc., 37, 263–297, https://doi.org/10.1146/annurev.earth.031208.100217, 2009.

Christensen, B. A., De Vleeschouwer, D., Henderiks, J., Groeneveld, J., Auer, G., Drury, A. J., Karatsolis, B. T., Lyu, J., Betzler, C., Eberli, G. P., and Kroon, D.: Late Miocene Onset of Tasman Leakage and Southern Hemisphere Supergyre Ushers in Near-Modern Circulation, Geophys. Res. Lett., 48, e2021GL095036, https://doi.org/10.1029/2021GL095036, 2021.

Cody, R. D., Levy, R. H., Harwood, D. M., and Sadler, P. M.: Thinking outside the zone: High-resolution quantitative diatom biochronology for the Antarctic Neogene, Palaeogeogr. Palaeocl., 260, 92–121, https://doi.org/10.1016/j.palaeo.2007.08.020, 2008.

Dearing Crampton-Flood, E., Peterse, F., and Sinninghe Damsté, J. S.: Production of branched tetraethers in the marine realm: Svalbard fjord sediments revisited, Org. Geochem., 138, 103907, https://doi.org/10.1016/j.orggeochem.2019.103907, 2019.

De Boer, A. M., Graham, R. M., Thomas, M. D., and Kohfeld, K. E.: The control of the Southern Hemisphere Westerlies on the position of the subtropical front, J. Geophys. Res.-Oceans, 118, 5669–5675, https://doi.org/10.1002/jgrc.20407, 2013.

De Vleeschouwer, D., Petrick, B. F., and Martínez-García, A.: Stepwise Weakening of the Pliocene Leeuwin Current, Geophys. Res. Lett., 46, 8310–8319, https://doi.org/10.1029/2019GL083670, 2019.

Ding, W. H., Yang, H., He, G. Q., and Xie, S.: Effects of oxidative degradation by hydrogen peroxide on tetraethers-based organic proxies, Quatern. Sci., 33, 39–47, https://doi.org/10.3969/j.issn.1001-7410.2013.01.05, 2013.

Duncan, B., McKay, R., Levy, R., Naish, T., Prebble, J. G., Sangiorgi, F., Krishnan, S., Hoem, F., Clowes, C., Dunkley Jones, T., Gasson, E., Kraus, C., Kulhanek, D. K., Meyers, S. R., Moossen, H., Warren, C., Willmott, V., Ventura, G. T., and Bendle, J.: Climatic and tectonic drivers of late Oligocene Antarctic ice volume, Nat. Geosci., 15, 819–825, https://doi.org/10.1038/s41561-022-01025-x, 2022.

Eglinton, T. I. and Eglinton, G.: Molecular proxies for paleoclimatology, Earth Planet. Sc. Lett., 275, 1–16, https://doi.org/10.1016/j.epsl.2008.07.012, 2008.

Evangelinos, D., Escutia, C., van de Flierdt, T., Valero, L., Flores, J. A., Harwood, D. M., Hoem, F. S., Bijl, P., Etourneau, J., Kreissig, K., Nilsson-Kerr, K., Holder, L., López-Quirós, A., and Salabarnada, A.: Absence of a strong, deep-reaching Antarctic Circumpolar Current zonal flow across the Tasmanian gateway during the Oligocene to early Miocene, Global Planet. Change, 208, 103718, https://doi.org/10.1016/j.gloplacha.2021.103718, 2022.

Exon, N. F., Kennett, J. P., Malone, M. J., and the Leg189 Shipboard Scientific Party: Site 1168, Proceedings of the Ocean Drilling Program Initial Reports, Ocean Drilling Program, College Station, TX, USA, http://www-odp.tamu.edu/publications/189_IR/chap_03/chap_03.htm (last access: 27 March 2023), 2001.

Freitas, F. S., Pancost, R. D., and Arndt, S.: The impact of alkenone degradation on $U_{37}^{K'}$ paleothermometry: A model-derived assessment, Paleoceanography, 32, 648–672, https://doi.org/10.1002/2016PA003043, 2017.

Gaskell, D. E., Huber, M., O'Brien, C. L., Inglis, G. N., Acosta, R. P., Poulsen, C. J., and Hull, P. M.: The latitudinal temperature gradient and its climate dependence as inferred from foraminiferal $\delta^{18}O$ over the past 95 million years, P. Natl. Acad. Sci. USA, 119, e2111332119, https://doi.org/10.1073/pnas.2111332119, 2022.

Gradstein, F. M. and Ogg, J, G.: The Chronostratigraphic Scale, in: Geologic Time Scale 2020, https://doi.org/10.1016/B978-0-12-824360-2.00002-4, 2020.

Gourley, T. L. and Gallagher, S. J.: Foraminiferal biofacies of the Miocene warm to cool climatic transition in the Port Phillip Basin, southeastern Australia, J. Foramin. Res., 34, 294–307, https://doi.org/10.2113/34.4.294, 2004.

Groeneveld, J., Henderiks, J., Renema, W., McHugh, C. M., de Vleeschouwer, D., Christensen, B. A., Fulthorpe, C. S., Reuning, L., Gallagher, S. J., Bogus, K., Auer, G., and Ishiwa, T.: Australian shelf sediments reveal shifts in Miocene Southern Hemisphere westerlies, Science Advances, 3, e1602567, https://doi.org/10.1126/sciadv.1602567, 2017.

Guitián, J. and Stoll, H. M.: Evolution of Sea Surface Temperature in the Southern Mid-latitudes From Late Oligocene Through Early Miocene, Paleoceanography and Paleoclimatology, 36, e2020PA004199, https://doi.org/10.1029/2020PA004199, 2021.

Hartman, J. D., Sangiorgi, F., Salabarnada, A., Peterse, F., Houben, A. J. P., Schouten, S., Brinkhuis, H., Escutia, C., and Bijl, P. K.: Paleoceanography and ice sheet variability offshore Wilkes Land, Antarctica – Part 3: Insights from Oligocene–Miocene TEX_{86}-based sea surface temperature reconstructions, Clim. Past, 14, 1275–1297, https://doi.org/10.5194/cp-14-1275-2018, 2018.

He, Y., Wang, H., and Liu, Z.: Development of the Leeuwin Current on the northwest shelf of Australia through the Pliocene-Pleistocene period, Earth Planet. Sc. Lett., 559, 116767, https://doi.org/10.1016/j.epsl.2021.116767, 2021.

Heath, R. A.: A review of the physical oceanography of the seas around New Zealand – 1982, New Zeal. J. Mar. Fresh., 19, 79–124, https://doi.org/10.1080/00288330.1985.9516077, 1985.

Herbert, T. D., Lawrence, K. T., Tzanova, A., Peterson, L. C., Caballero-Gill, R., and Kelly, C. S.: Late Miocene global cooling and the rise of modern ecosystems, Nat. Geosci., 9, 843–847, https://doi.org/10.1038/ngeo2813, 2016.

Hernández-Sánchez, M. T., Woodward, E. M. S., Taylor, K. W. R., Henderson, G. M., and Pancost, R. D.: Variations in GDGT distributions through the water column in the South East Atlantic Ocean, Geochim. Cosmochim. Ac., 132, 337–348, https://doi.org/10.1016/j.gca.2014.02.009, 2014.

Herold, N., Huber, M., and Müller, R. D.: Modeling the miocene climatic optimum. Part I: Land and atmosphere, J. Climate, 24, 6353–6372, https://doi.org/10.1175/2011JCLI4035.1, 2011.

Herold, N., Huber, M., Müller, R. D., and Seton, M.: Modeling the Miocene climatic optimum: Ocean circulation, Paleoceanography, 27, PA1209, https://doi.org/10.1029/2010PA002041, 2012.

Hoem, F. S., Sauermilch, I., Hou, S., Brinkhuis, H., Sangiorgi, F., and Bijl, P. K.: Late Eocene-early Miocene evolution of the southern Australian subtropical front: a marine palynological approach, J. Micropalaeontol., 40, 175–193, https://doi.org/10.5194/jm-40-175-2021, 2021.

Hoem, F. S., Sauermilch, I., Aleksinski, A. K., Huber, M., Peterse, F., Sangiorgi, F., and Bijl, P. K.: Strength and variability of the Oligocene Southern Ocean surface temperature gradient, Communications Earth and Environment, 3, 1–8, https://doi.org/10.1038/s43247-022-00666-5, 2022.

Ho, S. L. and Laepple, T.: Flat meridional temperature gradient in the early Eocene in the subsurface rather than surface ocean, Nat. Geosci., 9, 606–610, https://doi.org/10.1038/ngeo2763, 2016.

Holbourn, A., Kuhnt, W., Clemens, S., Prell, W., and Andersen, N.: Middle to late Miocene stepwise climate cooling: Evidence from a high-resolution deep water isotope curve spanning 8 million years, Paleoceanography, 28, 688–699, https://doi.org/10.1002/2013PA002538, 2013.

Hopmans, E. C., Weijers, J. W. H., Schefuß, E., Herfort, L., Sinninghe Damsté, J. S., and Schouten, S.: A novel proxy for terrestrial organic matter in sediments based on branched and isoprenoid tetraether lipids, Earth Planet. Sc. Lett., 224, 107–116, https://doi.org/10.1016/j.epsl.2004.05.012, 2004.

Hopmans, E. C., Schouten, S., and Sinninghe Damsté, J. S.: The effect of improved chromatography on GDGT-based palaeoproxies, Org. Geochem., 93, 1–6, https://doi.org/10.1016/j.orggeochem.2015.12.006, 2016.

Huguet, C., de Lange, G. J., Gustafsson, Ö., Middelburg, J. J., Sinninghe Damsté, J. S., and Schouten, S.: Selective preservation of soil organic matter in oxidized marine sediments (Madeira Abyssal Plain), Geochim. Cosmochim. Ac., 72, 6061–6068, https://doi.org/10.1016/j.gca.2008.09.021, 2008.

Hurley, S. J., Lipp, J. S., Close, H. G., Hinrichs, K. U., and Pearson, A.: Distribution and export of isoprenoid tetraether lipids in suspended particulate matter from the water column of the Western Atlantic Ocean, Org. Geochem., 116, 90–102, https://doi.org/10.1016/j.orggeochem.2017.11.010, 2018.

Jackson, C. A. L., Magee, C., and Hunt-Stewart, E. R.: Cenozoic contourites in the eastern great australian bight, offshore southern Australia: Implications for the onset of the Leeuwin Current, J. Sediment. Res., 89, 199–206, https://doi.org/10.2110/jsr.2019.16, 2019.

Kim, B. and Zhang, Y. G.: Methane hydrate dissociation across the Oligocene–Miocene boundary, Nat. Geosci., 15, 203–209, https://doi.org/10.1038/s41561-022-00895-5, 2022.

Kim, J. H., van der Meer, J., Schouten, S., Helmke, P., Willmott, V., Sangiorgi, F., Koç, N., Hopmans, E. C., and Damsté, J. S. S. New indices and calibrations derived from the distribution of crenarchaeal isoprenoid tetraether lipids: Implications for past sea surface temperature reconstructions, Geochim. Cosmochim. Ac., 74, 4639–4654, https://doi.org/10.1016/j.gca.2010.05.027, 2010.

Kim, J. H., Schouten, S., Rodrigo-Gámiz, M., Rampen, S., Marino, G., Huguet, C., Helmke, P., Buscail, R., Hopmans, E. C., Pross, J., Sangiorgi, F., Middelburg, J. B. M., and Sinninghe Damsté, J. S.: Influence of deep-water derived isoprenoid tetraether lipids on the TEX_{86}^{H} paleothermometer in the Mediterranean Sea, Geochim. Cosmochim. Ac., 150, 125–141, https://doi.org/10.1016/j.gca.2014.11.017, 2015.

Kim, J. H., Villanueva, L., Zell, C., and Sinninghe Damsté, J. S.: Biological source and provenance of deep-water derived isoprenoid tetraether lipids along the Portuguese continental margin. Geochim. Cosmochim. Ac., 172, 177–204, https://doi.org/10.1016/j.gca.2015.09.010, 2016.

Lear, C. H., Coxall, H. K., Foster, G. L., Lunt, D. J., Mawbey, E. M., Rosenthal, Y., Sosdian, S. M., Thomas, E., and Wilson, P. A.: Neogene ice volume and ocean temperatures: Insights from infaunal foraminiferal Mg / Ca paleothermometry, Paleoceanography, 30, 1437–1454, https://doi.org/10.1002/2015PA002833, 2015.

Leutert, T. J., Auderset, A., Martínez-García, A., Modestou, S., and Meckler, A. N.: Coupled Southern Ocean cooling and Antarctic ice sheet expansion during the middle Miocene, Nat. Geosci., 13, 634–639, https://doi.org/10.1038/s41561-020-0623-0, 2020.

Leutert, T. J., Modestou, S., Bernasconi, S. M., and Meckler, A. N.: Southern Ocean bottom-water cooling and ice sheet expansion during the middle Miocene climate transition, Clim. Past, 17, 2255–2271, https://doi.org/10.5194/cp-17-2255-2021, 2021.

Levy, R., Harwood, D., Florindo, F., Sangiorgi, F., Tripati, R., von Eynatten, H., Gasson, E., Kuhn, G., Tripati, A., DeConto, R., Fielding, C., Field, B., Golledge, N., McKay, R., Naish, T., Olney, M., Pollard, D., Schouten, S., Talarico, F., Warny, S., Willmott, V., Acton, G., Panter, K., Paulsen, T., Taviani, M., SMS Science Team, Acton, G., Askin, R., Atkins, C., Bassett, K., Beu, A., Blackstone, B., Browne, G., Ceregato, A., Cody, R., Cornamusini, G., Corrado, S., DeConto, R., Del Carlo, P., Di Vincenzo, G., Dunbar, G., Falk, C., Field, B., Fielding, C., Florindo, F., Frank, T., Giorgetti, G., Grelle, T., Gui, Z., Handwerger, D., Hannah, M., Harwood, D. M., Hauptvogel, D., Hayden, T., Henrys, S., Hoffmann, S., Iacoviello, F., Ishman, S., Jarrard, R., Johnson, K., Jovane, L., Judge, S., Kominz, M., Konfirst, M., Krissek, L., Kuhn, G., Lacy, L., Levy, R., Maffioli, P., Magens, D., Marcano, M. C., Millan, C., Mohr, B., Montone, P., Mukasa, S., Naish, T., Niessen, F., Ohneiser, C., Olney, M., Panter, K., Passchier, S., Patterson, M., Paulsen, T., Pekar, S., Pierdominici, S., Pollard, D., Raine, I., Reed, J., Reichelt, L., Riesselman, C., Rocchi, S., Sagnotti, L., Sandroni, S., Sangiorgi, F., Schmitt, D., Speece, M., Storey, B., Strada, E., Talarico, F., et al.: Antarctic ice sheet sensitivity to atmospheric CO_2 variations in the early to mid-Miocene, P. Natl. Acad. Sci. USA, 113, 3453–3458, https://doi.org/10.1073/pnas.1516030113, 2016.

Lewis, A. R., Marchant, D. R., Ashworth, A. C., Hemming, S. R., and Machlus, M. L.: Major middle Miocene global climate change: Evidence from East Antarctica and the Transantarctic Mountains, Geol. Soc. Am. Bull., 119, 1449–1461, https://doi.org/10.1130/b26134, 2007.

Liebrand, D., Lourens, L. J., Hodell, D. A., de Boer, B., van de Wal, R. S. W., and Pälike, H.: Antarctic ice sheet and oceanographic response to eccentricity forcing during the early Miocene, Clim. Past, 7, 869–880, https://doi.org/10.5194/cp-7-869-2011, 2011.

Marschalek, J. W., Zurli, L., Talarico, F., van de Flierdt, T., Vermeesch, P., Carter, A., Beny, F., Bout-Roumazeilles, V., Sangiorgi, F., Hemming, S. R., Pérez, L. F., Colleoni, F., Prebble, J. G., van Peer, T. E., Perotti, M., Shevenell, A. E., Browne, I., Kulhanek, D. K., Levy, R., Harwood, D., Sullivan, N. B., Meyers, S. R., Griffith, E. M., Hillenbrand, C.-D., Gasson, E., Siegert, M. J., Keisling, B., Licht, K. J., Kuhn, G., Dodd, J. P., Boshuis, C., De Santis, L., McKay, R. M., IODP Expedition 374, Ash, J., Beny, F., Browne, I. M., Cortese, G., De Santis, L., Dodd, J. P., Esper, O. M., Gales, J. A., Harwood, D. M., Ishino, S., Keisling, B. A., Kim, S., Kim, S., Kulhanek, D. K., Laberg, J. S., Leckie, R. M., McKay, R. M., Müller, J., Patterson, M. O., Romans, B. W., Romero, O. E., Sangiorgi, F., Seki, O., Shevenell, A. E., Singh, S. M., Cordeiro de Sousa, I. M., Sugisaki, S. T., van de Flierdt, T., van Peer, T. E., Xiao, W., and Xiong, Z.: A large West Antarctic Ice Sheet explains early Neogene sea-level amplitude, Nature, 600, 450–455, https://doi.org/10.1038/s41586-021-04148-0, 2021.

McGowran, B., Qianyu, L., Cann, J., Padley, D., McKirdy, D. M., and Shafik, S.: Biogeographic impact of the Leeuwin Current in southern Australia since the late middle Eocene, Palaeogeography, Palaeoclimatology, Palaeoecology, 136, 19–40, https://doi.org/10.1016/S0031-0182(97)00073-4, 1997.

McGowran, B., Holdgate, G. R., Li, Q., and Gallagher, S. J.: Cenozoic stratigraphic succession in southeastern Australia, Aust. J. Earth Sci., 51, 19–40, https://doi.org/10.1111/j.1400-0952.2004.01078.x, 2004.

McKay, R., Naish, T., Carter, L., Riesselman, C., Dunbar, R., Sjunneskog, C., Winter, D., Sangiorgi, F., Warren, C., Pagani, M., Schouten, S., Willmott, V., Levy, R., DeConto, R., and Powell, R. D.: Antarctic and Southern Ocean influences on Late Pliocene global cooling, P. Natl. Acad. Sci. USA, 109, 6423–6428, https://doi.org/10.1073/pnas.1112248109, 2012.

Meckler, A. N., Sexton, P. F., Piasecki, A. M., Leutert, T. J., Marquardt, J., Ziegler, M., Agterhuis, T., Lourens, L. J., Rae, J. W. B., Barnet, J., Tripati, A., and Bernasconi, S. M.: Cenozoic evolution of deep ocean temperature from clumped isotope thermometry, Science, 377, 86–90, https://doi.org/10.1126/science.abk0604, 2022.

Miller, K. G., Wright, J. D., and Fairbanks, R. G.: Unlocking the ice house: Oligocene-Miocene oxygen isotopes, eustasy, and margin erosion, J. Geophys. Res., 96, 6829–6848, https://doi.org/10.1029/90JB02015, 1991.

Modestou, S. E., Leutert, T. J., Fernandez, A., Lear, C. H., and Meckler, A. N.: Warm Middle Miocene Indian Ocean Bottom Water Temperatures: Comparison of Clumped Isotope and Mg / Ca-Based Estimates, Paleoceanography and Paleoclimatology, 35, e2020PA003927, https://doi.org/10.1029/2020PA003927, 2020.

Passchier, S., Browne, G., Field, B., Fielding, C. R., Krissek, L. A., Panter, K., and Pekar, S. F.: Early and middle miocene antarctic glacial history from the sedimentary facies distribution in the AND-2A drill hole, Ross sea, Antarctica, Bull. Geol. Soc. Am., 123, 2352–2365, https://doi.org/10.1130/B30334.1, 2011.

Peterse, F., Kim, J. H., Schouten, S., Kristensen, D. K., Koç, N., and Sinninghe Damsté, J. S.: Constraints on the application of the MBT/CBT palaeothermometer at high latitude environments (Svalbard, Norway), Org. Geochem., 40, 692–699, https://doi.org/10.1016/j.orggeochem.2009.03.004, 2009.

Pfuhl, H. A., Mccave, I. N., Schellenberg, S. A., and Ferretti, P.: Changes in Southern Ocean Circulation in Late Oligocene to Early Miocene Time, in: The Cenozoic Southern Ocean: Tectonics, Sedimentation, and Climate Change Between Australia and Antarctica, American Geophysical Union (AGU), 173–189, https://doi.org/10.1029/151GM11, 2004.

Prahl, F. G. and Wakeham, S. G.: Calibration of unsaturation patterns in long-chain ketone compositions for palaeotemperature assessment, Nature, 330, 367–369, https://doi.org/10.1038/330367a0, 1987.

Rae, J. W. B., Zhang, Y. G., Liu, X., Foster, G. L., Stoll, H. M., and Whiteford, R. D. M.: Atmospheric CO_2 over the past 66 million years from marine archives, Annu. Rev. Earth Pl. Sc., 49, 609–641, https://doi.org/10.1146/annurev-earth-082420-063026, 2021.

Ransom, B., Kim, D., Kastner, M., and Wainwright, S.: Organic matter preservation on continental slopes: importance of mineralogy and surface area, Geochim. Cosmochim. Ac., 62, 1329–1345, https://doi.org/10.1016/S0016-7037(98)00050-7, 1998.

Rintoul, S. R., Chown, S. L., DeConto, R. M., England, M. H., Fricker, H. A., Masson-Delmotte, V., Naish, T. R., Siegert, M. J., and Xavier, J. C.: Choosing the future of Antarctica, Nature, 558, 233–241, https://doi.org/10.1038/s41586-018-0173-4, 2018.

Robert, C.: Data Report: Bulk and Clay Mineral Assemblages of the Tasmanian Area, Maastrichtian–Pleistocene, ODP Leg 189, in: Proceedings of the Ocean Drilling Program, 189 Scientific Results, https://doi.org/10.2973/odp.proc.sr.189.114.2004, 2004.

Rousselle, G., Beltran, C., Sicre, M. A., Raffi, I., and de Rafélis, M.: Changes in sea-surface conditions in the Equatorial Pacific during the middle Miocene-Pliocene as inferred from coccolith geochemistry, Earth Planet. Sc. Lett., 361, 412–421, https://doi.org/10.1016/j.epsl.2012.11.003, 2013.

Rosell-Melé, A., Carter, J., and Eglinton, G.: Distributions of long-chain alkenones and alkyl alkenoates in marine surface sediments from the North East Atlantic, Org. Geochem., 22, 501–509, https://doi.org/10.1016/0146-6380(94)90122-8, 1994.

Sangiorgi, F., Bijl, P. K., Passchier, S., Salzmann, U., Schouten, S., McKay, R., Cody, R. D., Pross, J., van de Flierdt, T., Bohaty, S. M., Levy, R., Williams, T., Escutia, C., and Brinkhuis, H.: Southern Ocean warming and Wilkes Land ice sheet retreat during the mid-Miocene, Nat. Commun., 9, 1–11, https://doi.org/10.1038/s41467-017-02609-7, 2018.

Sangiorgi, F.: Miocene ocean temperatures (TEX86-L) of the ANDRILL-2A record, Ross Sea, Antarctica, PANGAEA [data set], https://doi.org/10.1594/PANGAEA.914002, 2020.

Sauermilch, I., Whittaker, J. M., Klocker, A., Munday, D. R., Hochmuth, K., Bijl, P. K., and LaCasce, J. H.: Gateway-driven weakening of ocean gyres leads to Southern Ocean cooling, Nat. Commun., 12, 6465, https://doi.org/10.1038/s41467-021-26658-1, 2021.

Scher, H. D., Whittaker, J. M., Williams, S. E., Latimer, J. C., Kordesch, W. E. C., and Delaney, M. L.: Onset of Antarctic Circumpolar Current 30 million years ago as Tasmanian Gateway aligned with westerlies, Nature, 523, 580–583, https://doi.org/10.1038/nature14598, 2015.

Schouten, S., Hopmans, E. C., Schefuß, E., and Sinninghe Damsté, J. S.: Distributional variations in marine crenarchaeotal membrane lipids: A new tool for reconstructing ancient sea water temperatures?, Earth Planet. Sc. Lett., 204, 265–274, https://doi.org/10.1016/S0012-821X(02)00979-2, 2002.

Schouten, S., Hopmans, E. C., and Sinninghe Damsté, J. S.: The organic geochemistry of glycerol dialkyl glycerol tetraether lipids: A review, Org. Geochem., 54, 19–61, https://doi.org/10.1016/j.orggeochem.2012.09.006, 2013.

Shevenell, A. E., Kennett, J. P., and Lea, D. W.: Middle Miocene Southern Ocean cooling and antarctic cryosphere expansion, Science, 305, 1766–1770, https://doi.org/10.1126/science.1100061, 2004.

Shevenell, A. E., Kennett, J. P., and Lea, D. W.: Middle Miocene ice sheet dynamics, deep-sea temperatures, and carbon cycling: A Southern Ocean perspective, Geochem. Geophy. Geosy., 9, Q02006, https://doi.org/10.1029/2007GC001736, 2008.

Sijp, W. P., von der Heydt, A. S., Dijkstra, H. A., Flögel, S., Douglas, P. M. J., and Bijl, P. K.: The role of ocean gateways on cooling climate on long time scales, Global Planet. Change, 119, 1–22, https://doi.org/10.1016/j.gloplacha.2014.04.004, 2014.

Sinninghe Damsté, J. S.: Spatial heterogeneity of sources of branched tetraethers in shelf systems: The geochemistry of tetraethers in the Berau River delta (Kalimantan, Indonesia), Geochim. Cosmochim. Ac., 186, 13–31, https://doi.org/10.1016/j.gca.2016.04.033, 2016.

Skinner, L. C., Fallon, S., Waelbroeck, C., Michel, E., and Barker, S.: Ventilation of the deep southern ocean and deglacial CO_2 rise, Science, 328, 1147–1151, https://doi.org/10.1126/science.1183627, 2010.

Sluijs, A., Frieling, J., Inglis, G. N., Nierop, K. G. J., Peterse, F., Sangiorgi, F., and Schouten, S.: Late Paleocene–early Eocene Arctic Ocean sea surface temperatures: reassessing biomarker paleothermometry at Lomonosov Ridge, Clim. Past, 16, 2381–2400, https://doi.org/10.5194/cp-16-2381-2020, 2020.

Sosdian, S. M., Greenop, R., Hain, M. P., Foster, G. L., Pearson, P. N., and Lear, C. H.: Constraining the evolution of Neogene ocean carbonate chemistry using the boron isotope pH proxy, Earth Planet. Sc. Lett., 498, 362–376, https://doi.org/10.1016/j.epsl.2018.06.017, 2018.

Stickley, C. E., Brinkhuis, H., McGonigal, K. L., Chaproniere, G. C. H., Fuller, M., Kelly, D. C., Nürnberg, D., Pfuhl, H. A., Schellenberg, S. A., Schoenfeld, J., Suzuki, N., Touchard, Y., Wei, W., Williams, G. L., Lara, J., and Stant, S. A.: Late Cretaceous–Quaternary Biomagnetostratigraphy of ODP Sites 1168, 1170, 1171, and 1172, Tasmanian Gateway, Proceedings of the Ocean Drilling Program, Scientific Results, 189, 1–57, https://doi.org/10.2973/odp.proc.sr.189.111.2004, 2004.

Super, J. R., Thomas, E., Pagani, M., Huber, M., O'Brien, C., and Hull, P. M. North Atlantic temperature and $p\mathrm{CO}_2$ coupling in the early-middle Miocene, Geology, 46, 519–522, https://doi.org/10.1130/G40228.1, 2018.

Super, J. R., Thomas, E., Pagani, M., Huber, M., O'Brien, C. L., and Hull, P. M.: Miocene Evolution of North Atlantic Sea Surface Temperature, Paleoceanography and Paleoclimatology, 35, 1–15, https://doi.org/10.1029/2019PA003748, 2020.

Tanner, T., Hernández-Almeida, I., Drury, A. J., Guitián, J., and Stoll, H.: Decreasing Atmospheric CO_2 During the Late Miocene Cooling, Paleoceanography and Paleoclimatology, 35, e2020PA003925, https://doi.org/10.1029/2020PA003925, 2020.

Taylor, K. W. R., Huber, M., Hollis, C. J., Hernandez-Sanchez, M. T., and Pancost, R. D.: Re-evaluating modern and Palaeogene GDGT distributions: Implications for SST reconstructions, Global Planet. Change, 108, 158–174, https://doi.org/10.1016/j.gloplacha.2013.06.011, 2013.

Tierney, J. E. and Tingley, M. P.: A Bayesian, spatially-varying calibration model for the TEX_{86} proxy, Geochim. Cosmochim. Ac., 127, 83–106, https://doi.org/10.1016/j.gca.2013.11.026, 2014.

Tierney, J. E. and Tingley, M. P.: A TEX_{86} surface sediment database and extended Bayesian calibration, Scientific Data, 2, 150029, https://doi.org/10.1038/sdata.2015.29, 2015.

Tierney, J. E. and Tingley, M. P.: BAYSPLINE: A New Calibration for the Alkenone Paleothermometer, Paleoceanography and Paleoclimatology, 33, 281–301, https://doi.org/10.1002/2017PA003201, 2018.

Toggweiler, J. R., Russell, J. L., and Carson, S. R.: Midlatitude westerlies, atmospheric CO_2, and climate change during the ice ages, Paleoceanography, 21, PA2005, https://doi.org/10.1029/2005PA001154, 2006.

Torsvik, T. H., van der Voo, R., Preeden, U., mac Niocaill, C., Steinberger, B., Doubrovine, P. v., van Hinsbergen, D. J. J., Domeier, M., Gaina, C., Tohver, E., Meert, J. G., McCausland, P. J. A., and Cocks, L. R. M.: Phanerozoic Polar Wander, Palaeogeography and Dynamics, Earth-Sci. Rev., 114, 3–4, https://doi.org/10.1016/j.earscirev.2012.06.007, 2012.

van der Weijst, C. M. H., van der Laan, K. J., Peterse, F., Reichart, G.-J., Sangiorgi, F., Schouten, S., Veenstra, T. J. T., and Sluijs, A.: A 15-million-year surface- and subsurface-integrated TEX_{86} temperature record from the eastern equatorial Atlantic, Clim. Past, 18, 1947–1962, https://doi.org/10.5194/cp-18-1947-2022, 2022.

Van Hinsbergen, D. J. J., de Groot, L. v., van Schaik, S. J., Spakman, W., Bijl, P. K., Sluijs, A., Langereis, C. G., and Brinkhuis, H.: A paleolatitude calculator for paleoclimate studies, PLoS ONE, 10, e0126946, https://doi.org/10.1371/journal.pone.0126946, 2015.

Volkman, J. K., Eglinton, G., Corner, E. D. S., and Forsberg, T. E. V.: Long-chain alkenes and alkenones in the marine coccolithophorid Emiliania huxleyi, Phytochemistry, 19, 2619–2622, https://doi.org/10.1016/S0031-9422(00)83930-8, 1980.

Weijers, J. W. H., Schouten, S., Spaargaren, O. C., and Sinninghe Damsté, J. S.: Occurrence and distribution of tetraether membrane lipids in soils: Implications for the use of the TEX_{86} proxy and the BIT index, Org. Geochem., 37, 1680–1693, https://doi.org/10.1016/j.orggeochem.2006.07.018, 2006.

Weijers, J. W. H., Lim, K. L. H., Aquilina, A., Damsté, J. S. S., and Pancost, R. D.: Biogeochemical controls on glycerol dialkyl glycerol tetraether lipid distributions in sediments characterized by diffusive methane flux, Geochem. Geophy. Geosy., 12, 1–15, https://doi.org/10.1029/2011GC003724, 2011.

Westerhold, T., Marwan, N., Drury, A. J., Liebrand, D., Agnini, C., Anagnostou, E., Barnet, J. S. K., Bohaty, S. M., De Vleeschouwer, D., Florindo, F., Frederichs, T., Hodell, D. A., Holbourn, A. E., Kroon, D., Lauretano, V., Littler, K., Lourens, L. J., Lyle, M., Pälike, H., Röhl, U., Tian, J., Wilkens, R. H., Wilson, P. A., and Zachos, J. C.: An astronomically dated record of Earth's climate and its predictability over the last 66 million years, Science, 369, 1383–1387, https://doi.org/10.1126/SCIENCE.ABA6853, 2020.

Wu, W., Xu, Y., Hou, S., Dong, L., Liu, H., Wang, H., Liu, W., and Zhang, C.: Origin and preservation of archaeal intact polar tetraether lipids in deeply buried sediments from the South China Sea, Deep-Sea Res.-Pt. I, 152, 103107, https://doi.org/10.1016/j.dsr.2019.103107, 2019.

Zhang, Y. G., Zhang, C. L., Liu, X. L., Li, L., Hinrichs, K. U., and Noakes, J. E.: Methane Index: A tetraether archaeal lipid biomarker indicator for detecting the instability of marine gas hydrates, Earth Planet. Sc. Lett., 307, 525–534, https://doi.org/10.1016/j.epsl.2011.05.031, 2011.

Zhang, Y. G., Pagani, M., and Liu, Z.: A 12-million-year temperature history of the tropical pacific ocean, Science, 344, 84–87, https://doi.org/10.1126/science.1246172, 2014.

Zhang, Y. G., Pagani, M., and Wang, Z.: Ring Index: A new strategy to evaluate the integrity of TEX_{86} paleothermometry, Paleoceanography, 31, 220–232, https://doi.org/10.1002/2015PA002848, 2016.

Zheng, Y., Heng, P., Conte, M. H., Vachula, R. S., and Huang, Y.: Systematic chemotaxonomic profiling and novel paleotemperature indices based on alkenones and alkenoates: Potential for disentangling mixed species input, Org. Geochem., 128, 26–41, https://doi.org/10.1016/j.orggeochem.2018.12.008, 2019.